CAMBRIDGE
UNIVERSITY PRESS

Research Article

Automatic detection of cataclysmic variables from SDSS images

Junfeng Huang[1] , Meixia Qu[1], Bin Jiang[1] , and Yanxia Zhang[2]

[1]School of Mechanical, Electrical & Information Engineering, Shandong University, Weihai, 264209, Shandong, China and [2]CAS Key Laboratory of Optical Astronomy, National Astronomical Observatories, Beijing, 100101, China

Abstract

Investigating rare and new objects have always been an important direction in astronomy. Cataclysmic variables (CVs) are ideal and natural celestial bodies for studying the accretion process of semi-detached binaries with accretion processes. However, the sample size of CVs must increase because a lager gap exists between the observational and the theoretical expanding CVs. Astronomy has entered the big data era and can provide massive images containing CV candidates. CVs as a type of faint celestial objects, are highly challenging to be identified directly from images using automatic manners. Deep learning has rapidly developed in intelligent image processing and has been widely applied in some astronomical fields with excellent detection results. YOLOX, as the latest YOLO framework, is advantageous in detecting small and dark targets. This work proposes an improved YOLOX-based framework according to the characteristics of CVs and Sloan Digital Sky Survey (SDSS) photometric images to train and verify the model to realise CV detection. We use the Convolutional Block Attention Module to increase the number of output features with the feature extraction network and adjust the feature fusion network to obtain fused features. Accordingly, the loss function is modified. Experimental results demonstrate that the improved model produces satisfactory results, with average accuracy (mean average *Precision* at 0.5) of 92.0%, *Precision* of 92.9%, *Recall* of 94.3%, and *F1 − score* of 93.6% on the test set. The proposed method can efficiently achieve the identification of CVs in test samples and search for CV candidates in unlabeled images. The image data vastly outnumber the spectra in the SDSS-released data. With supplementary follow-up observations or spectra, the proposed model can help astronomers in seeking and detecting CVs in a new manner to ensure that a more extensive CV catalog can be built. The proposed model may also be applied to the detection of other kinds of celestial objects.

Keywords: photometric images – cataclysmic variables – YOLOX – object detection

(Received 17 October 2022; revised 26 May 2023; accepted 20 June 2023)

1. Introduction

With the development of deep learning (DL), target detection algorithms have been applied in many fields and achieved state of the art results (LeCun et al., 2015). Meanwhile, the development of large survey telescopes, such as the Sloan Digital Sky Survey (SDSS; York et al. 2000) allows easier access to astronomical image data. Accordingly, target detection algorithms can be applied to massive astronomical images to provide celestial body detection by using the morphological structure and colour information contained in the images. Moreover, faint object detection in astronomical images can be technically solved. Cataclysmic variables (CVs) are a class of short-period binaries consisting of an accreting white dwarf (WD) primary star and a low-mass main-sequence secondary star as the mass donor (Warner, 2003). CVs can be classified into minor sub-types according to their amplitudes, timescale variability, and magnetism. CVs are also a class of periodic variables with complex spectral and orbital light curve variation (Hellier, 2001). CVs are a hot spot for astrophysical research due to their complex physical composition and variability, and are also a natural laboratory for studying accretion processes. Furthermore, CVs are the ideal objects for accretion

observations than other objects with accretion processes because of their close distances.

According to theoretical calculations, the Milky Way should have about 10 million CVs, but only 1829 CVs have been documented to date[a], of which only 1600 have been confirmed (Downes & Shara, 1993). This notion indicates the difficulty of discovering CVs and reflects the significance of searching for CVs.

Spectra can confirm CVs because they have strong emission lines, particularly during quiescence. Most optical spectra of CVs (Figure 1) show hydrogen Balmer emission lines, namely, 6563Å, 4862Å, 4341Å, 4102Å, and HeI 5876Å and HeII 4686Å during quiescence. Even conventional classification methods with prominent features can easily identify CVs from spectra. However, the number of spectra is limited due to the relatively high observation cost.

Photometric selection and brightness change is the most commonly used method in the search for CVs. CV candidates can be roughly selected out by photometric information and identified with spectra or follow-up observations. Wils et al. (2010) used the photometric selection criteria of $((u − g) + 0.85 * (g − r) < 0.18)$ to search for dwarf novas. Szkody et al. (2002, 2003, 2004, 2005, 2006, 2007, 2009) established a photometric selection criterion, i.e. $(u − g < 0.45, g − r < 0.7, r − i > 0.3, i − z > 0.4)$ to select WD-main sequence binaries with a few CVs and confirmed 285 CVs. These criteria overlap with quasars, faint blue galaxies, and WDs. In essence, there is no authorised criterion for CVs which is

Corresponding authors: Bin Jiang and Yanxia Zhang; E-mails: jiangbin@sdu.edu.cn, zyx@bao.ac.cn

[a]http://nesssi.cacr.caltech.edu/catalina/AllCV.arch.html

Figure 1. A CV spectrum from SDSS.

Figure 2. Some images from SDSS and CVs are at centre.

2. Data

The SDSS (York et al. 2000) provides a spectroscopic survey as well as a photometrically and astrometrically calibrated digital imaging survey. The photometric imaging includes five bands, namely, *u*, *g*, *r*, *i*, and *z* at the average wavelengths of 3551, 4686, 6165, 7481, and 8931Å, respectively. CVs are usually quite blue and faint objects. Our CV sample comes from Szkody et al. (2002, 2003, 2004, 2005, 2006, 2007, 2009), and duplicate CVs are deleted. We have uploaded the images of CVs to GitHub[b] for viewing. Appendix A displays the existing CV photometric data with spectra. We construct the CV sample with SDSS images already synthesised with *i*, *r*, and *g*-bands corresponding to the R, G, and B channels to more wildly apply our method. The images of CV samples have a size of 0.39612"/pix, some of which are shown in Figure 2.

2.1. Image preprocessing and data augmentation

First, the images are cleaned, the noise in the images are filtered, and a small amount of noisy images are removed, and 208 images are obtained, while can remove the interference of background noise to a certain extent. Given the small number of samples, the data set needs to be expanded using data enhancement methods, which not only guarantee the diversity of the data set but also improve the detection performance and enhances the robustness and generalisation ability of the model. Our method of using data augmentation is to generate a rotation angle within every 30 degrees randomly, rotate the image counterclockwise, and then randomly shift and crop respectively, and the ranges of shifting and cropping are shown in Table 1. We use the Lanczos interpolation (Thevenaz & Blu, 2000) to avoid voids on the image. Lanczos
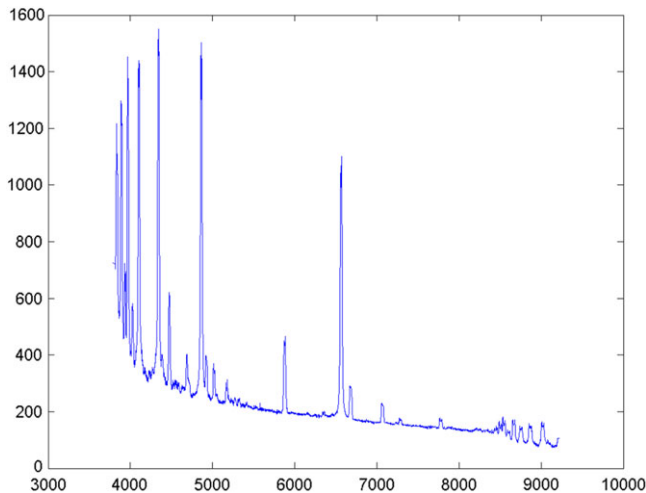
available at present. Drake et al. (2014) obtained 855 candidates from the Catalina Real-Time Transient Survey (Drake et al. 2011) by using the transient detection procedure. Mroz et al. (2016) received 1091 dwarf nova samples from the Optical Gravitational Lensing Experiment (Paczynski et al. 1995) by using the Early Warning System (Udalski, 2004) and photometric curve analysis. Han et al. (2018) found three new candidates by cross-matching the catalogs of CVs with the Large Sky Area Multi-Object Fiber Spectroscopic Telescope (LAMOST; Cui et al. 2012) DR3.

Traditional methods require a substantial amount of artificial time, sometimes years, to make follow-up observations. The manual techniques are not always accurate and frequently require many subjective judgements. With the simultaneous development of hardware and software in computer science, applying automated methods instead of manual methods can significantly increase efficiency and identification accuracy. Jiang & Luo (2011) obtained 58 CV candidates in SDSS by using the algorithm of PCA+SVM with massive spectra produced by LAMOST and SDSS. Hou et al. (2020) identified 58 new candidates by using bagging top push and random forest. Hu et al. (2021) found 225 candidates by using the LightGBM algorithm and verified four new CV candidates. Considering the quantitative limitation of spectra, applying a detector that can automatically identify CVs in images is demanding.

You Only Look Once (YOLO) is an object detection method. Its latest framework, YOLOX (Ge et al., 2021) can achieve fast detection and excellent image processing performance. However, the pixels occupied by CVs are extremely limited in astronomical images, resulting in low-resolution problems, blurred and less information, shallow features (brightness and edge), and weak expressiveness. Accordingly, we improve YOLOX to achieve low-cost, fast, and accurate localisation and identification of CVs. We train and validate the model using SDSS images for detecting CVs.

This paper is organised as follows. Section 2 introduces the data. Section 3 briefly illustrates YOLOX and our improvements to the current framework. Section 4 describes the data preprocessing and image enhancement, the experimental procedure, the experimental environment, and the evaluation of the experimental results. Section 5 discusses the experimental results. A comparison with previous research methods is also presented. Section 6 provides the conclusions and a summary of the study.

[b]https://github.com/Hickey-Curry/CVs-from-SDSS

Table 1. Randomly shifting and cropping range.

Operation	Scope name	Range
Shift	Horizontal range	[-tLeft/3, (iWidth-tRight)/3]
Shift	Vertical range	[-tTop/3, (iHeight-tBottom)/3]
Crop	Left border range	[0, tLeft]
Crop	Right border range	[tRight, iWidth]
Crop	Top border range	[0, tTop]
Crop	Bottom border range	[tBottom, iHeight]

tLeft, tRight, tTop, tBottom: the left, right, top, and bottom coordinates of the target in the image
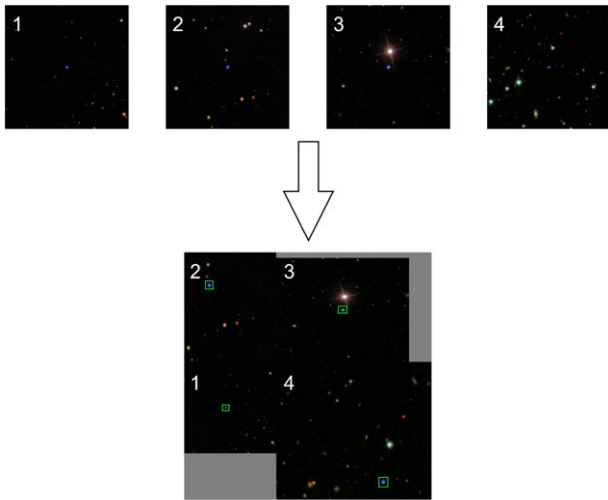
iWidth, iHeight: the width and height of the image

Figure 3. Data enhancement example by mosaic. Due to different size of each image, the blank is filled with grey colour when performing mosaic.

interpolation has the advantages of fast speed, good effect, and the most cost-effective. The methods of translation and clipping can enhance the position of the target, and the method of rotation can significantly change the orientation of the object without adding topological information.

In the YOLOX model training stage, the algorithm will also randomly enhance the data, the usual methods are Mosaic (Bochkovskiy et al., 2020) and Mixup (Zhang et al., 2017), Mosaic first randomly selects four images for conventional enhancement, and then stitches them into a new image, so that the new image contains the random target box information of the extracted image, and the random method maximises the rich data set. Mosaic enhances the diversity of data, enriches the background of the image, and also increases the number of targets, and the four images stitched together into the network improve the batch size, and the mean and variance can be better calculated when performing BN operations. A mosaic example is shown in Figure 3. The core idea of Mixup is to randomly select two images from each batch and superimpose a certain proportion to generate new images, reducing the memory of the model on the noisy samples, thereby reducing the impact of noisy samples on the model. A mixup example is shown in Figure 4.

2.2. Dataset

The external rectangular boxes of CVs in the image are drawn using the data set annotation software to achieve manual
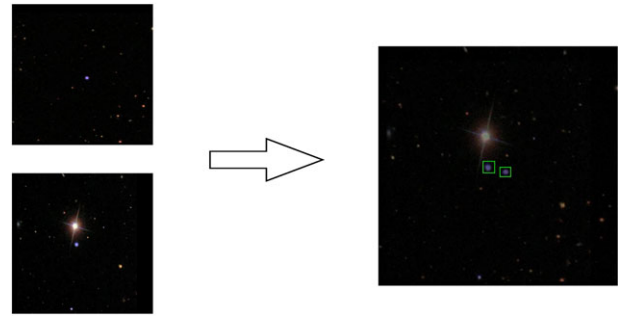

Figure 4. Data enhancement example by mixup.

annotation of CVs, ensuring that the rectangular boxes contain as little background as possible in the process. The annotated information is saved as XML format files and converted into TXT text by the program, while facilitates the data reading by the model.

After the data enhancement operation, a total number of 5200 images are achieved. From these images, 60% of images are randomly selected as training set, 20% as validation set, and the rest as test set. Finally, the dataset is made into Pascal VOC style. The training set is used to train the model (i.e., to determine the model weights and biases for these parameters). The validation set is only for selecting hyperparameters, such as the number of network layers, the number of network nodes, the number of iterations, and the learning rate. The test set is used to evaluate the final model after the training is completed.

3. Method

The definition of small targets in Computer Vision is as follows (Chen et al., 2016): the median ratio of the target of the same category relative to the whole image area is between 0.08% and 0.58%. The most common definition is from the MS COCO (Lin et al., 2014) dataset, which defines a small target as a resolution of fewer than 32×32 pixels. According to the International Society for Optical Engineering definition, an imaging area of fewer than 80 pixels in a 256×256 image is a small target. CV detection can thus be considered a detection task for small targets. Small targets contain little information, making it challenging to extract discriminative features. Existing DL methods for small target detection include multi-scale learning, contextual learning, adding attention mechanisms, generating super-resolution feature representations, anchorless mechanisms, and optimising loss-type handling disparity datasets. YOLO uses an end-to-end neural network that makes predictions of bounding boxes and class probabilities appropriate for CV detection. YOLOX is an anchor-free version of YOLO, with a more straightforward design but better performance. The attention mechanism allows the network to focus on what needs more attention. Adding the attention module to YOLO can effectively enhance the network's ability to capture the image's features. Convolutional Block Attention Module (CBAM; Woo et al. 2018) is a simple and effective attention module for feedforward convolutional neural networks because of its lightweight and versatility and can be seamlessly integrated into YOLOX. The following introduces YOLOX and CBAM in detail. Inspired from these directions, we propose an improved CV object detection model.
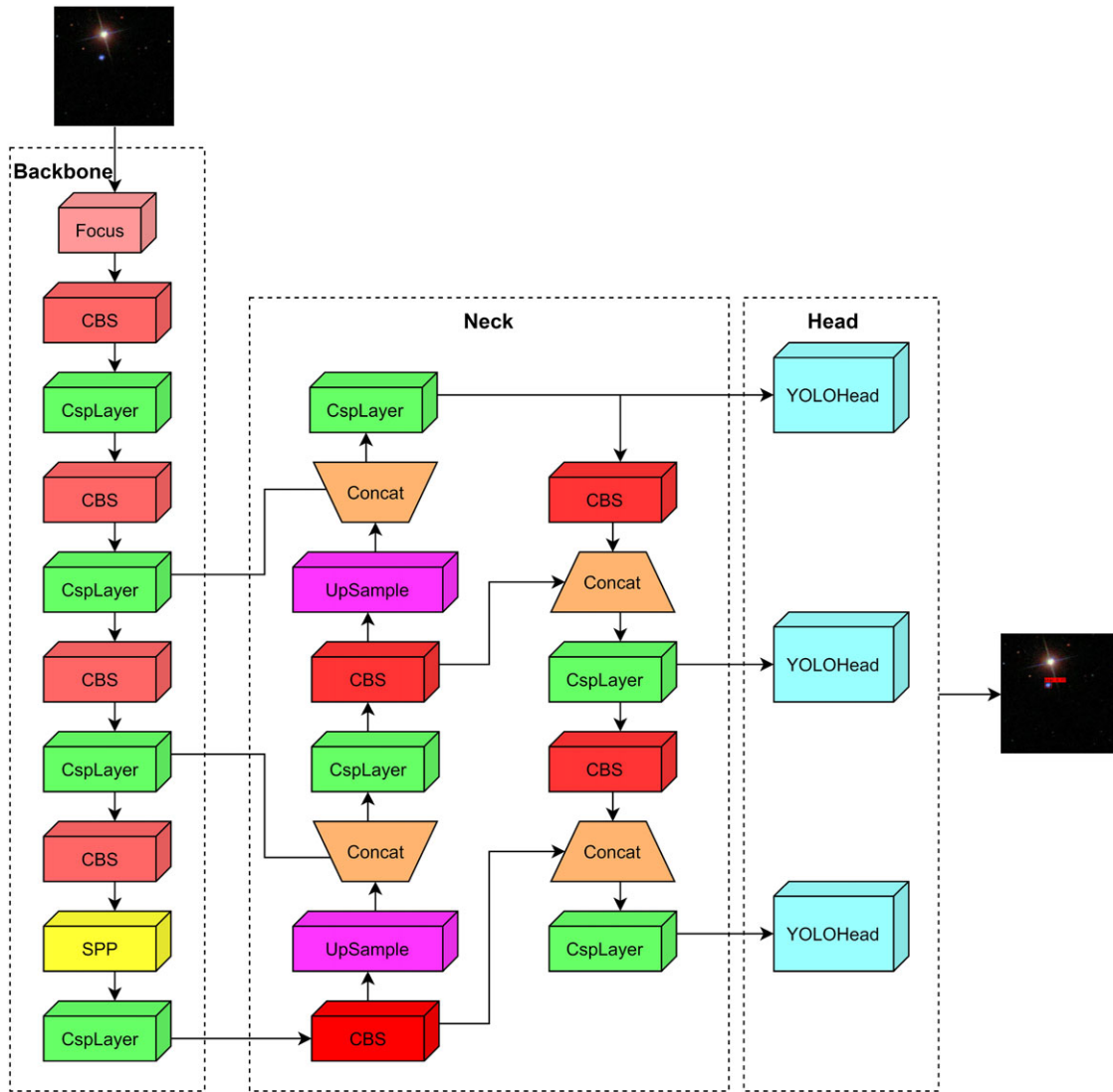
Figure 5. The architecture of YOLOX.

3.1. YOLOX

YOLOX uses CSPDarkNet (Bochkovskiy et al., 2020) as the backbone following the filter size and overall structure of DarkNet (Redmon & Farhadi, 2017), adding a cross-stage partial structure to each residual block (He et al., 2016). Figure 5 shows the architecture of YOLOX.

YOLOX is a network composed of a feature pyramid network (FPN; (FPN; Deng et al. 2022) with a pixel aggregation network (PAN; (PAN;Wang et al. 2022), which is a fusion of high-level features by upsampling and low-level features to obtain a new feature map. Meanwhile, PAN fuses low-level features by downsampling and containing features further to pass up the robust localisation features. The final following feature maps of multi-scale features are obtained, which are used to detect large, medium, and small targets. YOLOX feeds the enhanced feature map into the head network for classification and localisation. Unlike the previous versions of YOLOX, YOLOX uses a decoupled head structure. The head structure is divided into two parts, namely, classification and localisation, which are separately implemented and then

integrated into the final prediction stage. YOLOX proposes the SimOTA technique to dynamically match positive samples for targets of different sizes. The loss function of the YOLOX algorithm typically includes target, classification, and regression losses. Binary cross-entropy and IOU loss are used in target classification and regression separately. Classification and regression loss calculates the loss of positive samples. Meanwhile, target loss calculates the loss of positive and negative samples.

3.2. CBAM

CBAM is a simple and effective attention module for feed-forward convolutional neural networks. This module processes the input feature map, derives the attention map along two separate dimensions, channel and space, and applies the result into the input feature map. The channel attention mechanism (CAM) uses parallel AvgPool and MaxPool approaches to process the input. The parallel connection approach loses less information than a single pooling; hence, this approach has more symbolic power. The CAM in CBAM differs from SEnet by adding a parallel max-pooling
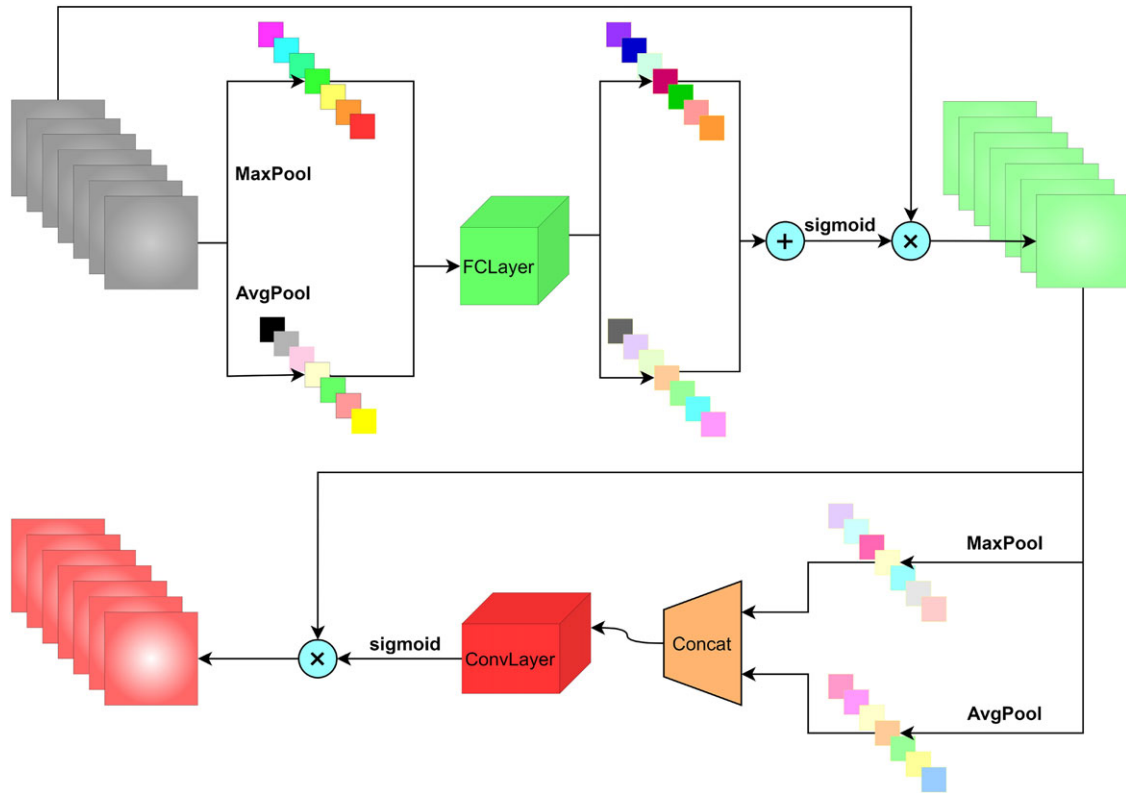
Figure 6. The basic structure and processing flow chart of CBAM.

layer, which extracts more comprehensive and richer high-level features. The spatial attention mechanism (SAM) also uses parallel AvgPool and MaxPool approaches. Unlike CAM which sums two 1D attention data, SAM uses a convolutional approach to dimensionally compress the attention graph, which more effectively preserves the spatial information in the feature graph. Finally, CBAM combines the two modules, CAM and SAM, in a serial sequential way according to the ablation experiment.

The CBAM module can be inserted into YOLOX and helps the fusion of multi-scale features, by reducing the weights, and CBAM filters the factor that is detrimental to the model's recognition ability, thus improving the network's performance with only a small additional computational cost. Figure 6 shows the processing flow chart of CBAM.

3.3. Improved method

To make the YOLOX more suitable for identifying and localising CVs in images, we apply the following improvements: 1) The attention module of CBAM is adopted to direct the network's attention on the important information of the target. 2) The number of output feature maps of the backbone is adjusted for small targets, adding a shallow feature map and inputting four feature maps into the improved FPN+PAN network for fusion. 3) Considering the overlap area, centroid distance, and aspect ratio between the prediction result and the actual target box, the CIOU (Zheng et al., 2021) loss for the regression loss is adopted. Accordingly, problems, such as performance degradation of YOLOX, are also addressed.

Specifically, we use CBAM to combine the channel and SAMs. Each channel can be considered a feature detector for the feature map. The CAM compresses the feature map in the spatial dimension to obtain a thought vector and then process it. The CAM focuses on what is essential in this image, and the mean pooling has feedback for each pixel point on the feature map. Although maximum pooling has feedback for gradients when performing gradient backpropagation, only the places in the feature map with the most significant response have feedback for gradients. The SAM is more concerned with where the essential parts are, and it compresses the channel dimension of the feature map to ensure that a two-channel feature map can be obtained for subsequent processing. The CBAM attention mechanism is a simple and effective attention module for feedforward convolutional neural networks because of its lightweight and versatility and can be seamlessly integrated into any network. The CBAM module can be inserted into YOLOX networks to more effectively mine CV features carried in astronomical images, which helps the fusion of multi-scale features, thus improving the performance of the network with a small additional computational cost.

In the convolutional neural network, the fewer the convolution operations, the lower the output feature map, the smaller the receptive field, the higher resolution of the feature map and the smaller the target features are retained. Using low-level feature maps is beneficial to the detection efficiency of small objects. We increase the number of output feature maps of the backbone network, add the feature maps after the 10th layer convolution operation to the output results, and enter the four feature maps into the improved FPN+PAN network for multi-scale feature fusion to ensure that the final fusion of three. This new feature
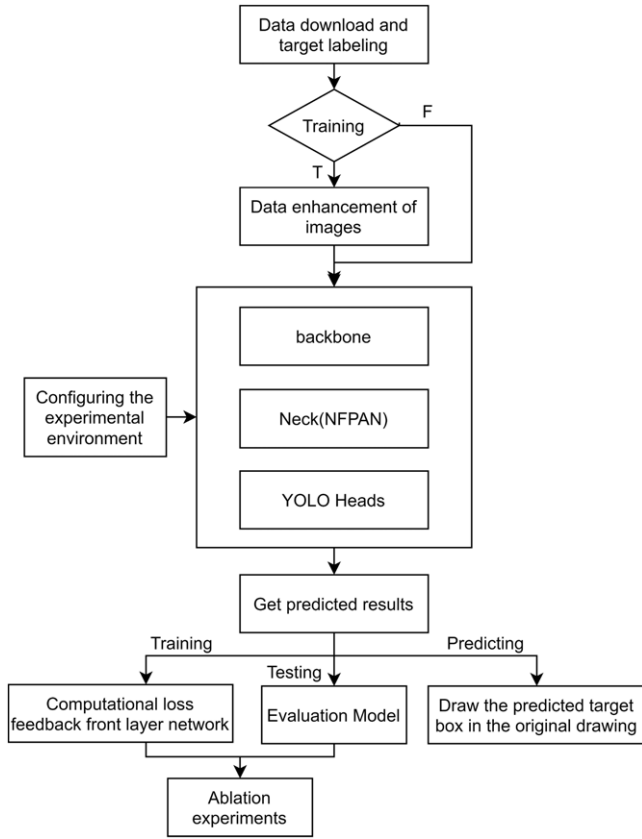
Figure 7. The proposed pipeline.

Table 2. Results of ablation experiments.

Method	mAP@0.5	mAP[0.5:0.95]	Precision	Recall	F1-Score
YOLOX	89.2%	34.6%	91.9%	94.3%	93.1%
+CBAM	88.6%	33.2%	90.8%	92.3%	91.5%
+NFPAN	90.1%	35.6%	92.3%	94.1%	93.2%
+CIOU	90.2%	35.3%	92.4%	94.2%	93.3%
+CBAM+NFPAN	90.4%	34.7%	91.7%	93.7%	92.7%
+CBAM+CIOU	91.6%	34.7%	93.1%	94.6%	93.8%
+NFPAN+CIOU	90.4%	34.0%	92.4%	94.0%	93.2%
+CBAM+NFPAN+CIOU	92.0%	35.4%	92.9%	94.3%	93.6%

Table 3. Comparison of mAP, *Precision*, *Recall*, and $F1 - Score$ of our improved YOLOX model with the original YOLOX model and LightGBM.

Method	mAP@0.5	mAP[0.5:0.95]	*Precision*	*Recall*	$F1 - Score$
LightGBM with spectra			95.21%	93.53%	94.36%
YOLOX with images	89.20%	34.60%	91.90%	94.30%	93.10%
Our improved YOLOX with images	92.00%	35.40%	92.90%	94.30%	93.60%

Table 4. Model speed evaluation for 10 times.

Frequency	Second	FPS
1	0.03239	30.876
2	0.03215	31.106
3	0.03264	30.635
4	0.03314	30.171
5	0.03221	31.048
6	0.03192	31.329
7	0.03416	29.274
8	0.03210	31.154
9	0.03129	31.957
10	0.03163	31.615

map contains more small target features. Although the calculation amount of the fusion process increases, it is beneficial to the future identification and positioning of CVs.

$$IOU = \frac{intersection}{union}. \tag{1}$$

The loss function makes the detection more accurate and localisation more precise, reflecting the error between the prediction result of the detection algorithm and the actual target. IOU loss (Yu et al., 2016) is normally used in the regression to measure the degree of overlap. In Formula 1, this factor can efficiently respond to the degree of overlap and provide a scale without deformation. We use CIOU loss as the regression loss, considering the overlap area, centroid distance, and aspect ratio to more stably optimise the model. The model can more accurately locate CVs, and its calculation is shown in Formulas 2, 3, and 4, where b and b^{gt} denote the centre coordinates of the prediction and true boxes respectively; d denotes the Euclidean distance between the centre coordinates of the prediction and true boxes; c denotes the diagonal distance of the minimum external matrix of the prediction and true boxes; w and w^{gt} denote the width of the prediction and true boxes, respectively; and h and h^{gt} denote the height of the prediction and true boxes, respectively.

$$CIOU = IOU - \frac{\rho^2(b, b^{gt})}{c^2} - \alpha v, \tag{2}$$

$$\alpha = \frac{v}{(1 - IOU) + v}, \tag{3}$$

$$v = \frac{4}{\pi^2} \left(arctan \frac{w^{gt}}{h^{gt}} - arctan \frac{w}{h} \right)^2. \tag{4}$$

4. Experiment

The flowchart of the whole procedure is shown in Figure 7. The preparation for annotating images and data enhancement is introduced in Section 4.1, and this step is required during the training model phase. The environment is set up before conducting the experiments in Section 4.5. Afterwards, we use the improved model to obtain prediction results. In the training model phase, the model parameters need to be improved based on the resulting deviations. In the test phase, the results are used to evaluate the effectiveness of the model using the evaluation criteria adopted in Section 4.2. In the prediction phase, the prediction target boxes are drawn based on the results. Ablation experiments in Section 4.3 are performed to verify the effectiveness of each improved model based on the training and test results.

4.1. Evaluation index

We use Mean Average Precision (mAP; (mAP; Everingham et al. 2015), *Precision*, *Recall*, and *F1 − Score* as experimental metrics. *Precision* is the proportion of correct results among all predicted targets. Meanwhile, *Recall* is the proportion of correct results relative to all true targets. The calculation methods are shown in Formulas 5 and 6, where *TP* is the number of predicted bounding boxes with IOUs greater than the threshold value, *FP* is the number of predicted bounding boxes with IOUs less than or equal to the threshold value, and *FN* is the number of predicted bounding boxes that do not match the true target box. Setting different thresholds can result in distinct (P, R) values, refracting the (P, R) values corresponding to different thresholds on a 2D coordinate system and connecting them into a curve. The mAP is the average of AP of each category, and AP is the area under the P-R curve. As shown in Formula 7, *F1 − Score* is the summed average of *Precision* and *Recall*.

In target detection, mAP is the most convincing evaluation index. We use the YOLO algorithm corresponding to the mAP@0.5 and mAP [0.5:0.95] to evaluate our model. mAP@0.5 is the average of all categories of AP and mAP [0.5:0.95] is to set the IOU thresholds as 0.5, 0.55, 0.6, 0.65, 0.7, 0.75, 0.8, 0.9, and 0.95 when averaged. The higher mAP of a model, the better the corresponding detection will be.

$$Precision = \frac{TP}{TP + FP}, \tag{5}$$

$$Recall = \frac{TP}{TP + FN}, \tag{6}$$

$$F1 - Score = 2 \times \frac{Precision \times Recall}{Precision + Recall}. \tag{7}$$

In order to reflect the fast speed of the model, the common indicator for evaluating speed in object detection is frame rate per second (FPS), that is, the target network can process the number of pictures per second, FPS is simply understood as the refresh rate of the image, that is, how many frames per second, assuming that the target detection network processes 1 frame to 0.02 s, at this time FPS is $1/0.02 = 50$. We train the model in the same hardware environment that evaluates the monitoring speed using the time it takes to process an image. The shorter the time, the faster the speed is.

4.2. Ablation study

We apply three modules to improve YOLOX for small target detection. The three modules can be summarised as adding CBAM, adding feature maps to FPN+PAN, and adjusting the regression loss to CIOU. We perform an ablation study on the model to verify the contribution of the three modules to the detection improvement, and all experimental data sets and hyperparameter configurations are the same as before. Table 2 shows the experimental results. In comparison with the original YOLOX, mAP is improved by adding NFPAN module or CIOU module. Meanwhile, mAP is decreased by only adding CBAM module. However, the results from adding CBAM and CIOU modules show that CBAM is effective based on CIOU. According to the results of the three groups with adding the two

modules, CIOU is more significant to improve the performance than NFPAN or CBAM. Considering all the three modules, the performance of the model is the best. Therefore the improvement of our model is effective in identifying CVs.

4.3. Experimental results

We compare the performance of the YOLOX models with the classification model of Hu et al. (2021) using the LightGBM algorithm. The mAP, *Precision*, *Recall*, and *F1 − Score* of the three models are shown in Table 3. Hu et al. (2021) used LightGBM from the LAMOST-DR7 spectra to automatically search for CV candidates, which extracts the potential relationships concerning CV spectra. LightGBM combines multiple features to prevent the interference of individual features by noise and finally achieves 95.21% *Precision*, 93.53% *Recall*, and 94.36% *F1 − Score*. The model's classification performance is excellent because spectra contain more abundant information than images, and the data processing is fast due to the small model. LightGBM is a classification model that only works with spectra. The YOLOX models can achieve CV recognition and localisation in astronomical images, especially the improved YOLOX model with 92.9% *Precision*, 94.3% *Recall*, and 93.6% *F1 − Score*. The target detection algorithm is to classify and regress each pixel point on the extracted feature map. Accordingly, the task of the target detection model will be more complicated than the classification model, and the accuracy will be reduced only based on images. Nonetheless, the target detection algorithm will be more advantageous for massive astronomical images when spectral observation is expensive. Figures 8 and 9 show the effect of the detection of CVs in the images. The cases where the predicted results differ from the ground truth are shown in Table 5.

To evaluate the deviation of the results detected by our model from the actual results, we calculate the pixel distance between the predicted results of the model and the centre of the actual target on the test set, because we use an image of 0.39612"/pix, and the final result of the experiment is that the centre mean arcsecond deviation is 0.8058".

We select an image from the dataset to evaluate the speed of the model. We test it for 10 times under the same hardware conditions to calculate the FPS, and the results are shown in Table 4. The final result averages them, and the FPS of our model is 30.9165.

4.4. Experimental environment

Tables 6 and 7 show the software and hardware environment of the experiment and the hyperparameters used for model training. Given that we use 16 samples as a batch size when training the model and the network's depth is deep, we use NVIDIA GeForce RTX 3070 for acceleration. Furthermore, PyTorch calls to take advantage of a complete graphics card for complex parallel computing. In the training stage, the frozen training method can speed up the efficiency of model training and prevent the weights from being destroyed. In the freezing stage, the backbone network of the model is frozen, the parameters of the feature extraction network do not change, and the memory usage is negligible. In this stage, only the network is fine-tuned. In the thawing stage, the backbone network of the model is not frozen, and all competitions in the network will change, occupying a large amount of GPU memory.
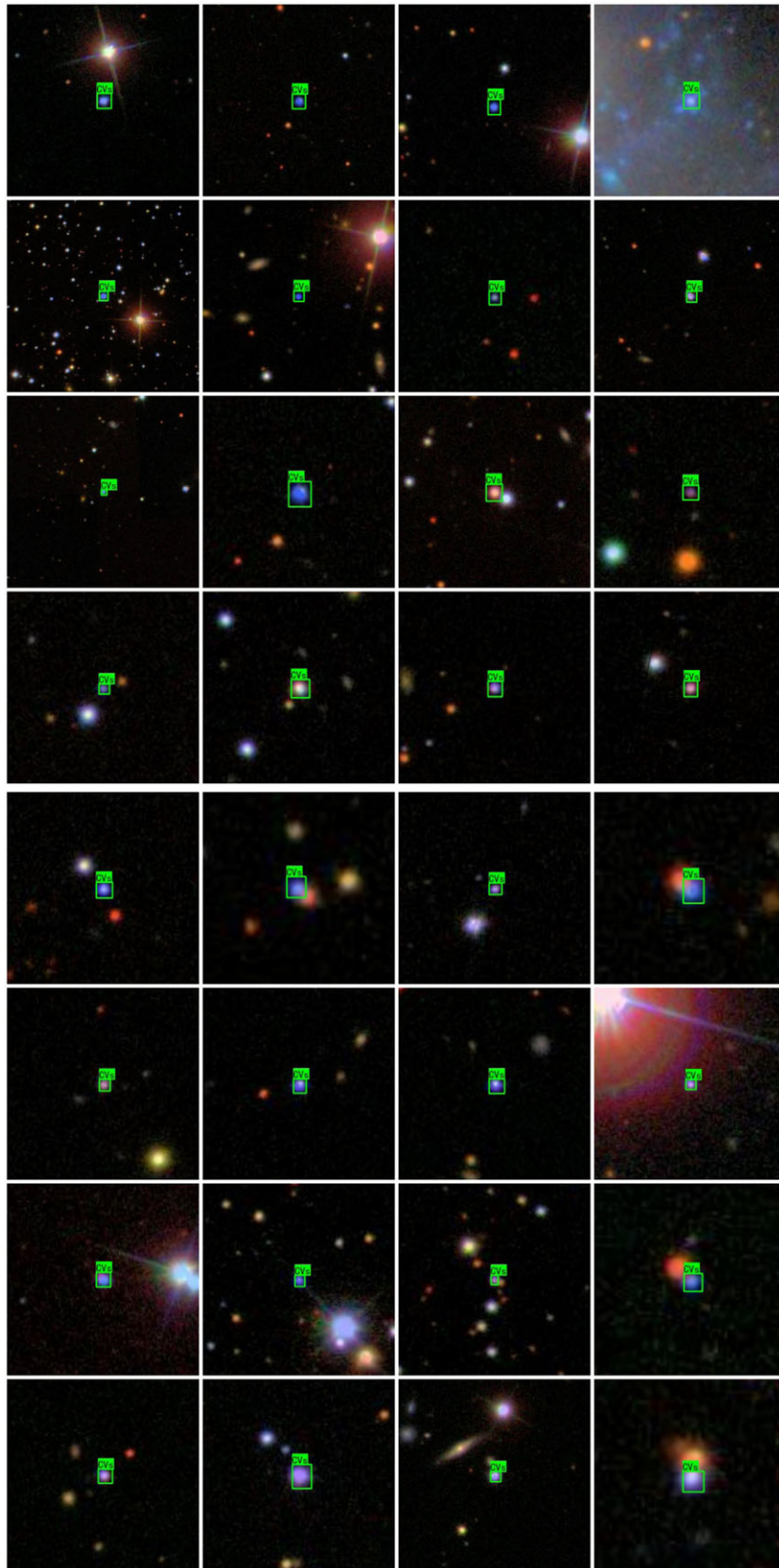
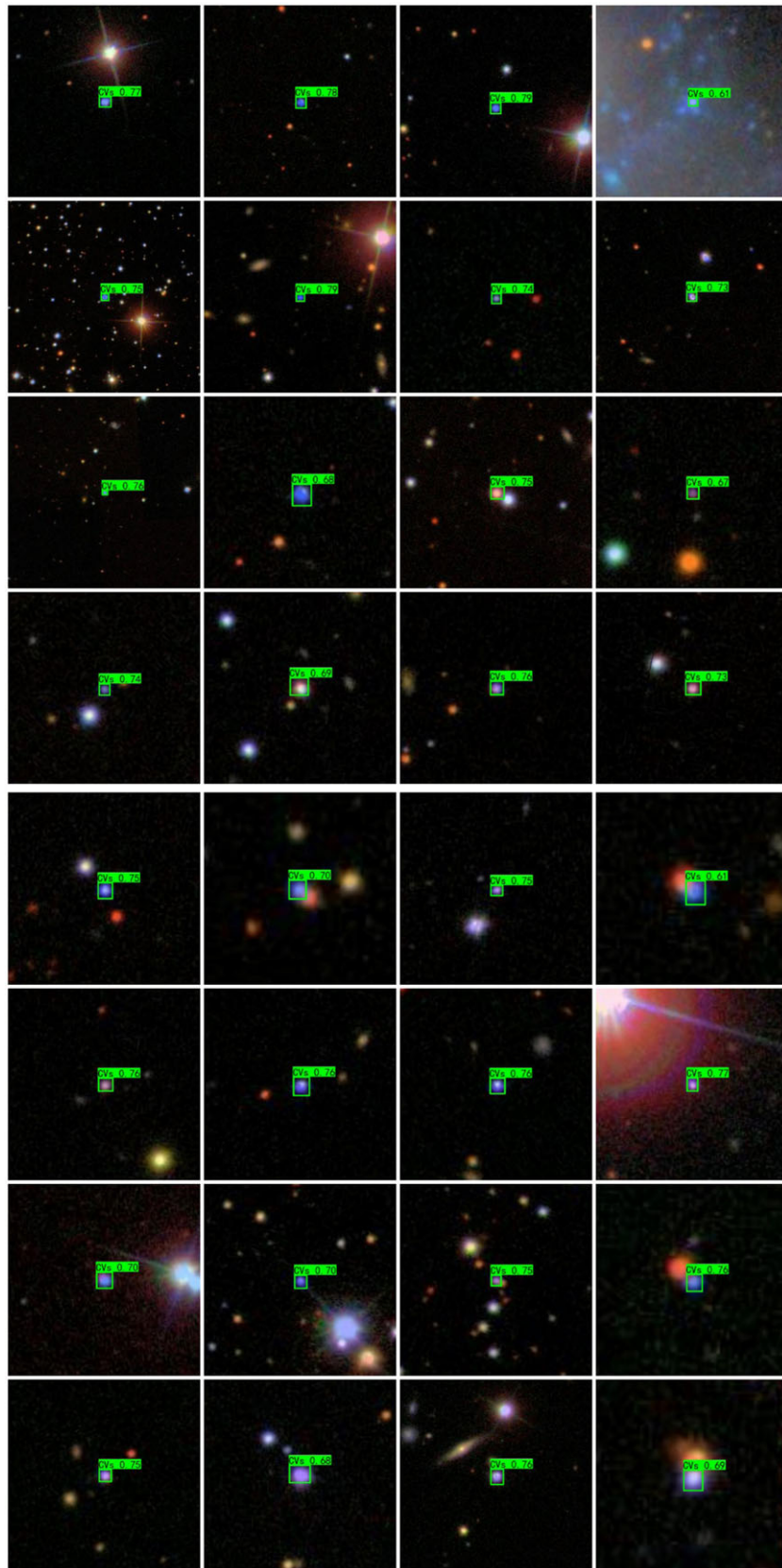**Figure 8.** Ground truth of the image samples from SDSS.

Figure 9. Predicted image samples from SDSS.

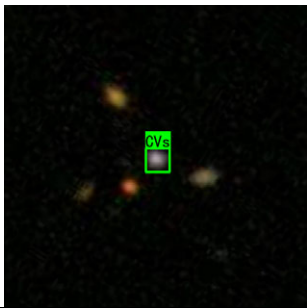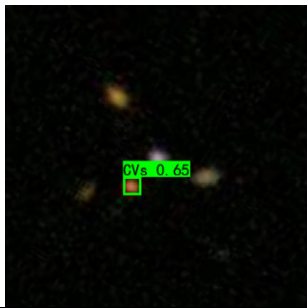**Table 5.** The cases where the predicted results differ from the ground truth.
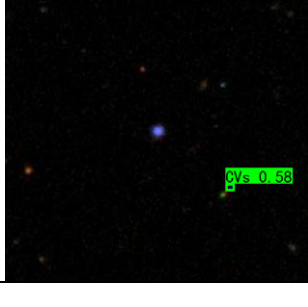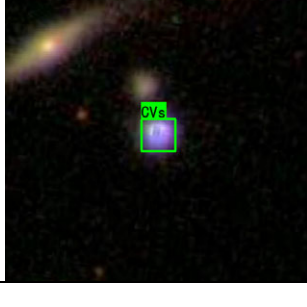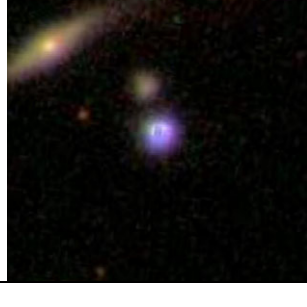
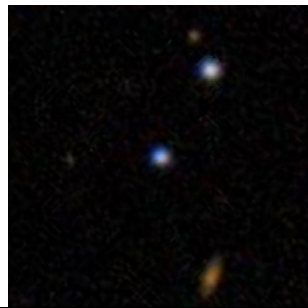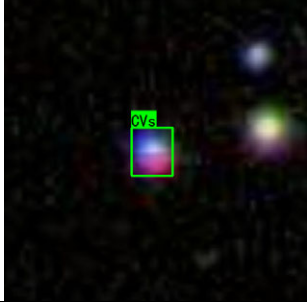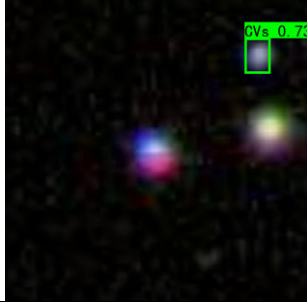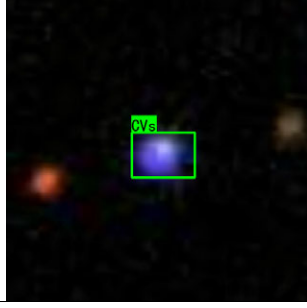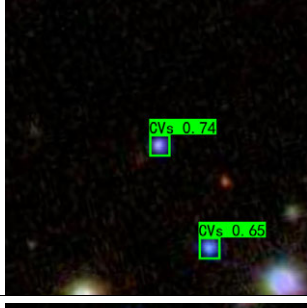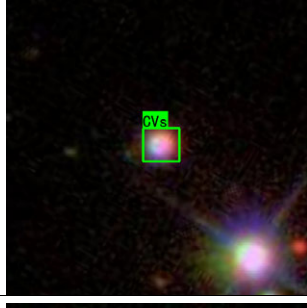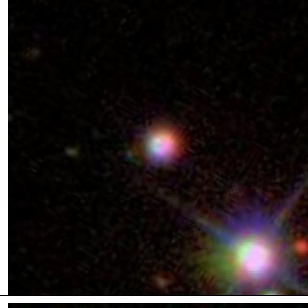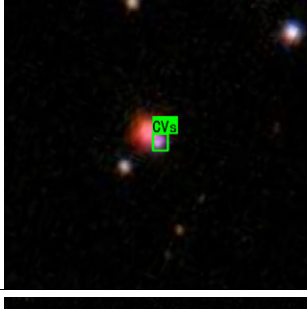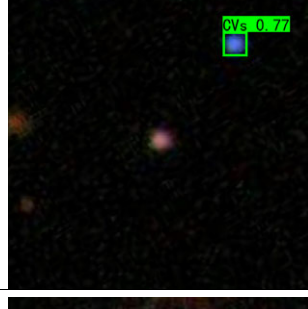| Ground truth images (SDSS)	Predicted images (SDSS)	Ground truth images (SDSS)	Predicted images (SDSS)

Table 6. Experimental environment.

Placements	Values
Graphics Processing Unit	$8 \times 3\,070$
Operating System	18.04.1
Programming Language	Python 3.7.6
Machine Learning Library	Pytorch 1.8.1
Operational Platform	CUDA 11.1

Table 7. Hyperparameters of the improved YOLOX model.

Hyperparameters	Values
Batch Size	16
Freeze Epoch	50
UnFreeze Epoch	150
Init Learning Rate	0.01
Optimiser	SGD
Momentum	0.937

5. Discussion

The experimental results illustrate that the improved CV detection model can effectively localise and classify CVs in images. In the face of massive astronomical images, our model takes shorter time with satisfactory accuracy, which is crucial for fully using the observation data produced by large survey telescopes.

Considering the vast amount of astronomical images, we choose the fast and accurate YOLOX target detection algorithm to achieve the localisation and recognition of astronomical images. To address the problem that the DL algorithm degrades in accuracy when facing small targets, YOLOX is improved by adding an attention mechanism, adjusting the backbone output and the FPN+PAN network structure, switching to a suitable loss function, and applying data enhancement methods according to the characteristics of astronomical images. These improvements enhance the adaptability and effectiveness of the model for the CV detection task.

For existing supervised learning methods, the images of the corresponding objects must be recollected to train the model when identifying and locating other types of objects. Most DL algorithms lose accuracy when faced with small targets. Our model needs further improvement to cope up with this degradation to improve accuracy.

The YOLOX target detection model can localise and identify all CVs in the image and complete the detection of all targets. However, our model only tests the case with one CV in the image because each astronomical image we download contains only one object. In the future, we will further investigate scenes with multiple targets in the image. Our method will be improved by further optimising the loss function and neural network architecture to enhance our model's classification and localisation performance for small target objects. We will also enhance the model's performance by considering the background of CVs in astronomical images and extracting rich available features. In addition, different types of astronomical objects will be extended to increase the amount of data available to us.

Accordingly, the improved models can locate, detect, and classify CVs simultaneously and are easy to encapsulate into the software. We will further strengthen the learning ability of the network by combining other observed CV data (e.g., spectroscopic and infrared data) with image data for analysis. When processing astronomical data, we will also consider cross-matching data from different astronomical telescopes and fusing the features of other data to improve the accuracy of our model. Another exciting improvement direction is to fully use the fast target detection function of YOLOX to achieve classification and localisation of CVs from images generated by ordinary telescopes. We will also consider how to better exploit our model's localisation property in astronomical image recognition.

6. Conclusions

We propose an improved CV detector based on the YOLOX framework for the automatic identification and localisation of CVs to take advantage of astronomical images conveniently. This tool is helpful for the discovery of CVs, for the subsequent study of their physical composition and change mechanisms, and research on the accretion process in astrophysics. For the characteristics of astronomical optical images, we improve YOLOX by adding an attention mechanism and backbone output feature maps to make the fused features more multi-scale, adjusting the appropriate loss function, and adopting data enhancement. The experiments prove that the improved model performs better than the original YOLOX and demonstrate our model's accuracy and robustness for processing optical images observed by astronomical telescopes to identify and localise CVs in the images. The actual use of test sets to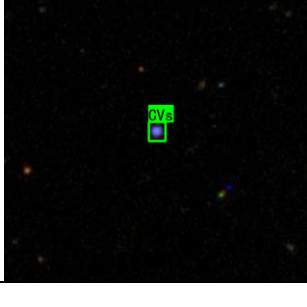 judge the model confirms that the performance of the improved model is superior to that of the original algorithm, and the improved model has higher accuracy and robustness while ensuring detection speed. This mechanism will further facilitate astronomers' research and improve the accuracy of models and the reliability of judgments. The relevant toolkit is under development. We used Flask+Vue for rapid modern web application development, and built a simple user interface of CV detection toolkit, shown in Figures B1 and B2 in Appendix B. This toolkit will make our research more accessible for astronomers, and we hope to see more exciting and new discoveries of CVs or other kinds of celestial objects by means of it.

Lawrence Berkeley National Laboratory, Leibniz Institut für Astrophysik Potsdam (AIP), Max-Planck-Institut für Astronomie (MPIA Heidelberg), Max-Planck-Institut für Astrophysik (MPA Garching), Max-Planck-Institut für Extraterrestrische Physik (MPE), National Astronomical Observatories of China, New Mexico State University, New York University, University of Notre Dame, Observatário Nacional/MCTI, The Ohio State University, Pennsylvania State University, Shanghai Astronomical Observatory, United Kingdom Participation Group, Universidad Nacional Autónoma de México, University of Arizona, University of Colorado Boulder, University of Oxford, University of Portsmouth, University of Utah, University of Virginia, University of Washington, University of Wisconsin, Vanderbilt University, and Yale University.

References

Bochkovskiy, A., Wang, C. Y., & Liao, H. 2020

Chen, C., Liu, M.-Y., Tuzel, O., & Xiao, J. 2016, in Asian Conference on Computer Vision, Springer, 214–230

Cui, X.-Q., Zhao, Y.-H., Chu, Y.-Q., et al. 2012, RAA, 12, 1197

Deng, C., Wang, M., Liu, L., Liu, Y., & Jiang, Y. 2022, IEEE Trans. Multimed., 24, 1968

Downes, R. A., & Shara, M. M. 1993,, 105, 127

Drake, A. J., Djorgovski, S. G., Mahabal, A., et al. 2011, Proc. Int. Astronom. Union, 7, 306

Drake, A. J., Gänsicke, B., Djorgovski, S. G., et al. 2014, MNRAS, 441, 1186

Everingham, M., Eslami, S. A., Van Gool, L., et al. 2015, IJCV, 111, 98

Ge, Z., Liu, S., Wang, F., Li, Z., & Sun, J. 2021

Han, X. L., Zhang, L.-Y., Shi, J.-R., et al. 2018, RAA, 18, 068

He, K., Zhang, X., Ren, S., & Sun, J. 2016, IEEE

Hellier, C. 2001, Springer Verlag

Hou, W., Luo, A. L., Li, Y. B., & Qin, L. 2020, AJ, 159, 43

Hu, Z., Chen, J., Jiang, B., & Wang, W. 2021, Universe, 7, 438

Jiang, B., & Luo, A. L. 2011, Spectrosc. Spectr. Anal.

LeCun, Y., Bengio, Y., & Hinton, G. 2015, Nature, 521, 436

Lin, T. Y., Maire, M., Belongie, S., Hays, J., & Zitnick, C. L. 2014, Springer International Publishing

Mroz, P., Udalski, A., Poleski, R., et al. 2016, AcA, 65

Paczynski, B., Stanek, K. Z., Udalski, A., Szymanski, M., & Preston, G. W. 1995, BAAS

Redmon, J., & Farhadi, A. 2017, in IEEE Conference on Computer Vision & Pattern Recognition, 6517–6525

Szkody, P., Anderson, S. F., Agüeros, M., et al. 2002, The Astronomical Journal, 123, 430

Szkody, P., Fraser, O., Silvestri, N., et al. 2003, AJ, 126, 1499

Szkody, P., Henden, A., Fraser, O., et al. 2004, AJ, 128, 1882

Szkody, P., Henden, A., Fraser, O. J., et al. 2005, AJ, 129, 2386

Szkody, P., Henden, A., Agüeros, M., et al. 2006, AJ, 131, 973

Szkody, P., Henden, A., Mannikko, L., et al. 2007, AJ, 134, 185

Szkody, P., Anderson, S. F., Hayden, M., et al. 2009, AJ, 137, 4011

Thevenaz, P., & Blu, T. 2000, IEEE Trans. Med. Imag., 19, 739

Udalski, A. 2004, AcA -Warsaw and Cracow-, 53

Wang, W., Xie, E., Li, X., et al. 2022, IEEE Trans. Patt. Anal. Mach. Intell., 44, 5349

Warner, B. 2003, Cataclysmic Variable Stars, doi: 10.1017/CBO9780511586491

Woo, S., Park, J., Lee, J.-Y., & Kweon, I. S. 2018, in Proceedings of the European Conference on Computer Vision (ECCV), 3–19

York, D. G., Adelman, J., Anderson Jr, J. E., et al. 2000, AJ, 120, 1579

York, D. G., Adelman, J., Anderson, JOHN E., J., et al. 2000, 120, 1579

Yu, J., Jiang, Y., Wang, Z., Cao, Z., & Huang, T. 2016, ACM

Zhang, H., Cisse, M., Dauphin, Y. N., & Lopez-Paz, D. 2017

Zheng, Z., Wang, P., Ren, D., et al. 2021, IEEE Trans. Cybernet.

Appendix A. The CV photometric data

Ra,Dec	u	g	r	i	z
157.35429, 61.47645	22.81	22.35	21.68	22.12	22.28
127.37297, 0.22334	21.97	21.91	21.79	22.03	22.8
139.1829, 61.40397	21.15	21.07	21.2	20.99	20.16
265.38723, 68.07786	20.04	20.51	20.13	19.96	19.58
240.94201, 19.59443	16.62	16.73	16.49	15.82	15.44
340.26559, 5.09127	23.93	21.9	21.15	20.7	20.57
14.54622, −1.13078	22.55	22.02	21.75	21.93	21.31
244.25382, 62.00675	16.43	16.14	16.21	16.35	16.41
201.92153, 22.13333	22.21	21.48	21.28	21.23	21.12
210.51295, 46.22611	19.86	19.5	19.64	19.89	20.1
198.63381, 44.69418	15.1	15.08	15.26	15.44	15.62
340.04916, 30.3215	22.59	22.76	22.33	22.57	21.86
172.51287, 28.11336	22.32	22.34	21.82	22.63	22.11
236.71982, 37.90417	16	16.02	16.27	16.46	16.66
245.9603, −12.292	19.85	19.69	19.25	18.74	18.21
256.52558, 25.86482	21.23	21.48	21.31	21.21	21.04
237.62627, −0.23824	21.9	22.01	21.61	21.03	20.77
248.69424, 32.31199	22.44	22.72	23.85	23.91	22.92
240.68923, 2.68499	25.32	21.9	21.57	21.39	21.11
182.52214, −2.92893	21.09	20.87	21	21.28	20.63
239.33644, 18.12231	18.28	18.64	18.67	18.32	18.19
194.04202, 62.618	21.81	21.53	21.5	21.44	20.75
78.72064, 60.52053	21.48	20.75	20.48	20.33	20.23
113.35608, 37.62914	22.13	21.88	22.08	22.47	21.71
162.30021, 51.44737	20.43	20.36	20.22	20.27	20.26
120.14108, 19.40458	19.92	20.13	20.04	19.96	19.69
114.7416, 10.64936	20.47	20.97	20.59	20.64	20.46
136.52683, 0.07643	22.09	21.92	21.77	22.32	23.11
127.77684, −5.71164	18.66	19.03	18.92	18.64	18.5
143.42164, 58.77056	23.43	22.46	22.36	22.05	21.69
75.11366, 13.57226	19.22	18.59	17.56	16.53	15.75
117.24807, 31.4202	15.85	15.75	15.89	16.01	16.11
61.12081, 20.05015	18.29	17.87	17.79	17.72	17.67
322.02557, 2.53915	22.52	22.51	22.65	22.28	22.72
317.57352, 9.05054	23.74	23.58	23	22.83	22.53
25.17008, −8.38629	20.13	19.55	19.3	19.39	18.95
82.12907, 1.53334	23.42	22.05	21.18	20.87	20.43
338.25205, 31.88274	22.14	22.37	22.52	22.15	21.16
340.04687, 10.36606	20.7	20.83	20.58	20.63	21.04
19.05219, 32.64427	20.31	20.48	20.32	20.17	19.88
325.72648, 15.61174	23.02	22.56	22.69	23.09	22.67
321.2572, 6.79359	22.12	21.04	20	19.71	19.39
16.78955, −9.85855	21.69	21.52	21.28	21.35	21.69
231.28996, 36.01507	19.63	19.83	20.06	20.3	20.43
9.1492, 21.85718	22.64	21.58	21.54	22.09	22.72
350.1094, 22.30929	21.5	21.07	21.1	21.27	20.78
325.34574, 7.99811	22.15	21.88	21.48	21.21	21.19

Ra,Dec	u	g	r	i	z	Ra,Dec	u	g	r	i	z
339.79314, 5.09785	22.71	21.1	19.67	18.74	18.12	137.50687, 16.80539	18.47	18.83	18.54	18.54	18.33
220.87615, 8.20583	21.04	21.32	21.23	21.18	21.81	170.01407, 66.60894	15.81	15.61	15.9	16.12	16.33
252.52887, 39.4654	24.1	22.57	23.73	22.39	22.35	118.22898, 53.09197	21.25	21.55	21.4	21.71	21.7
319.90391, 3.5367	21.3	20.16	19.34	18.91	18.6	118.24271, −0.11922	23.01	23.39	22.43	21.84	21.17
331.21605, −2.13321	22.62	22.45	22.27	21.98	21.48	150.67982, −2.7762	21.16	21.37	21.51	21.19	20.48
314.15716, 2.97845	24.39	22.87	21.58	19.97	19.22	24.42141, 22.05338	23.4	20.82	19.07	18.25	17.82
129.58152, 16.8442	21.01	21.01	20.91	20.81	19.94	188.10744, 14.34507	15.49	15.3	15.49	15.61	15.73
180.67016, 29.84176	22.48	22.98	22.3	22.81	21.64	75.48273, 13.83266	24.33	24.04	23.07	22.39	22.12
262.856, 27.90787	21.61	21.86	21.58	21.9	21.76	353.94146, 12.58011	19.93	19.66	19.25	18.59	18.08
123.83378, 17.72896	20.8	21.23	20.93	20.76	20.37	321.55312, 3.89605	21.43	21.59	21.58	21.79	21.15
131.57006, 31.26549	22.41	21.81	21.6	21.39	21.27	11.54089, 35.26099	22.04	22.39	22.42	22.2	22
36.09366, 21.22439	20.11	20.27	19.89	19.89	19.46	133.25246, 2.0737	14.97	14.98	15.23	15.47	15.71
146.52889, −0.93382	20.37	20.43	20.26	20.09	19.59	127.48942, −1.03373	21.97	22.23	21.98	22.58	22.43
123.6057, 20.35713	21.78	22.06	21.78	21.74	21.82	16.76624, 42.72006	19.4	19.62	19.31	18.88	18.36
190.8679, −5.90876	23.19	22.7	22.56	22.29	21.79	14.42091, 44.51699	21.12	20.94	21.06	21.18	21.07
31.40666, 26.71786	19.51	19.38	19.6	19.36	18.7	9.26659, 14.20279	20.29	20.03	20.14	20.09	20.05
117.78123, 30.1079	19.55	19.78	19.82	19.84	19.77	50.36905, 18.14086	23.16	23.16	21.54	18.59	17.03
118.70897, 9.17199	21.06	21.19	21.13	21.19	21.01	81.05061, 0.69669	18.51	18.32	17.81	17.37	17
114.49397, 20.92902	17.2	17.4	17.22	17.28	17.27	129.88051, 28.47339	20.01	20.23	20.17	20.05	19.52
344.83734, 27.92977	25.12	22.43	20.84	19.77	19.08	52.91474, 4.53392	22.45	19.19	17.75	17.17	16.74
23.01164, −10.73257	20.28	20.82	20.35	20.56	20.42	10.77337, 37.05902	19.36	19.56	19.24	19.23	19.18
47.37417, 26.63455	19.14	18.88	18.91	19.01	18.97	13.44725, 40.93014	18.59	18.14	17.78	17.61	17.5
116.19143, 40.23026	25.16	23.08	21.74	20.63	20.22	350.47904, 32.06875	23.07	20.82	20.02	20.66	19.3
25.76954, 26.6425	17.6	17.91	17.91	17.71	17.59	267.11625, 50.84446	19.84	19.86	19.83	19.52	19.17
24.19086, −19.66363	18.01	19.81	18.23	18.32	18.63	37.41801, −3.10567	20.31	20.76	20.49	20.63	20.3
52.52611, 18.20918	21.73	21.32	20.46	20.2	19.89	354.59385, −20.83113	21.69	21.59	21.39	21.72	20.69
38.61586, −4.90858	16.42	16.26	16.37	16.55	16.63	314.53332, −0.83232	22.82	22.72	22.66	22.37	22.48
259.57704, 29.59554	17.88	17.66	17.9	18.09	18.22	347.05658, 25.72818	19.63	19.81	19.55	19.39	19.07
4.81591, 15.75567	23.07	22.95	22.1	22.38	22.28	253.0055, 24.77525	21.05	19.31	18.67	18.4	18.27
319.1491, −7.81958	22.5	22.2	21.87	22.07	23.16	29.30083, 22.73397	22.16	21.91	21.76	21.58	21.35
231.9502, 35.62038	20.53	20.85	20.26	20.08	19.8	319.08914, 8.78705	21.64	21.75	21.09	20.69	20.2
356.78344, 30.84358	22.34	22.8	22.34	21.95	21.75	315.06675, −2.7161	20.92	19.85	19.64	19.5	19.34
253.38296, −5.16564	23.33	22.7	21.91	21.7	22.01	7.73256, 23.2961	22.37	22.24	22.33	22.2	22.28
330.86755, 30.94361	19.46	19.6	19.34	19.15	19.03	313.21983, −2.66467	18.15	18.34	18.25	18.36	18.36
255.02147, −11.07134	21.73	21.21	20.11	19.45	18.89	334.05755, 1.68507	21.82	22.9	23.14	23.17	23.36
254.43932, −4.73468	25.39	22.63	20.99	20.2	19.62	320.80641, −2.24644	22.15	22.12	21.93	22.49	22.13
217.40107, 32.44168	20.96	21.33	20.67	20.34	20.28	312.03783, 0.97767	22.72	22.69	22.44	22.18	22.61
252.01148, 12.35569	24.44	22.93	22.41	21.91	21.87	265.25688, 26.90029	20.76	20.65	20.32	20.21	20.35
149.64973, 28.18177	21.5	21.47	21.43	21.31	20.51	266.44717, 26.72972	18.16	18.41	18.3	18.37	18.17
251.77799, 62.41419	18.29	18.14	18.34	18.45	18.6	318.94732, 16.19886	25.44	22.55	22.33	22.84	21.58
266.67854, 50.18645	22.78	22.02	20.59	19.51	18.94	327.33823, 21.06279	20.5	20.8	20.53	20.51	20.63
262.69834, 55.75493	19.81	19.73	19.68	19.48	19.19	216.47854, −22.63482	26.29	21.83	21.66	21.45	22.91
213.03345, 10.23522	21.29	21.17	21.35	21.42	21.4	349.04841, 27.58069	20.39	20.38	20.46	20.71	20.46
259.83859, 64.05279	21.41	21.29	21.25	21.3	21.93	328.61328, 15.95384	18.75	18.64	18.62	18.5	18.42
112.10353, 38.6991	22.12	21.24	20.47	20.14	20.17	209.17679, 61.50702	21.65	21.26	21.35	20.97	20.44
121.75439, 55.79416	20.62	20.6	20.37	20.4	20.43	168.1493, 0.47051	22.11	22.46	22.13	22.42	21.5
123.53511, 9.13311	20.58	20.69	20.47	19.96	19.42	152.97884, 14.19224	21.3	21.56	21.31	21.13	21.2
169.21867, 1.24346	21.96	21.81	21.81	21.55	21.31	146.99926, 6.17894	20.04	20.42	20.19	20.27	20.26

Ra,Dec	u	g	r	i	z	Ra,Dec	u	g	r	i	z
223.97281, 11.47115	20.41	20.78	20.24	19.73	19.29	254.42072, −5.94016	20.61	20.07	19.45	19.11	18.78
117.83652, 31.782	22.32	22.15	22.28	22.87	22.17	129.07911, 21.35139	17.19	16.77	16.57	16.48	16.43
131.14727, 53.07531	22.41	22.01	21.92	21.57	21.13	258.20786, 31.11877	21.44	20.95	20.02	19.14	18.61
192.94498, 41.05027	23.47	24.26	22.56	21.71	21.25	194.77408, 24.44289	20.67	21.11	21.16	20.92	20.83
166.80663, 13.56004	21.63	21.84	21.74	21.9	21.13	167.86195, 57.21081	18.93	19.22	19.26	19.28	19.38
253.15116, 46.08749	21.97	22.1	21.87	21.29	20.85	191.82944, 1.64531	20.62	20.77	20.92	21.09	20.71
227.26558, 46.84929	21.36	20.98	20.71	20.54	20.16	247.74523, 11.72422	21.85	22.27	21.97	21.8	21.65
117.82081, 10.00458	17.88	18.49	18.37	18.39	18.33	225.20544, −8.74638	19.04	19.19	19.13	18.93	18.67
113.57772, 27.21929	19.82	20.29	19.96	19.81	19.78	233.71298, 7.49183	21.24	23.07	21.2	21.18	21.76
123.63153, 42.26656	22.18	21.89	21.94	22.36	22.04	241.04402, 14.93839	21.86	21.7	21.72	22.02	21.89
136.5474, 24.28318	25.19	24.77	23.87	21.94	21.59	167.40662, 50.6581	20.38	20.88	20.84	20.68	20.32
118.57799, 38.20694	22.69	22.75	23.01	22.98	21.75	198.80988, 42.79636	17.24	17.03	17.22	17.37	17.51
235.79344, 4.92529	22.88	22.39	21.93	21.72	21.2	147.22483, 1.81968	20.7	20.71	20.6	20.75	20.56
188.862, 16.50874	21.99	22	21.79	22.24	21.87	135.06896, 43.02174	18.69	18.88	18.19	17.51	17.02
171.58099, 8.78083	22.2	21.83	21.84	22.28	21.31	113.03389, 41.50258	16.38	16.19	16.5	16.67	16.8
162.60809, 33.47032	22.74	22.53	22.29	22.56	22.63	194.15471, 26.61202	17.92	17.94	17.89	17.87	17.68
141.66121, 36.40073	18.73	18.96	19.2	19.39	19.42	145.85783, 52.02466	17.75	18.32	18.37	18.15	17.92
65.57448, 33.70419	19.94	19.79	18.82	18.15	17.73	237.07312, 15.53926	21.59	21.83	21.74	21.89	21.76
69.87491, −4.60007	15.12	14.6	14.29	14.16	14.11	140.34494, 20.64948	20.7	19.85	19.17	19.17	19.43
31.6394, 20.95205	15.66	15.55	15.49	15.6	15.68	191.50847, −20.38399	18.36	18.53	18.41	18.35	18.27
144.94176, 6.86942	17.49	17.25	17.59	17.7	17.88	123.15231, 16.32931	21.95	22.17	22.26	22.08	21.89
21.41404, 32.38569	13.34	12.99	13.07	13.34	13.64	181.58267, −3.4773	19.73	19.93	19.98	20	19.64
349.74074, −6.04633	21.13	21.32	21.21	21.45	21.53	235.09359, 1.37532	24.17	22.08	21.52	21.2	20.77
270.20418, 52.54313	20.33	20.54	20.18	19.95	19.55	12.58574, 33.32159	16.77	16.57	16.76	16.94	17.08
47.71529, −7.91665	15.76	15.48	15.74	15.89	16.1	122.42237, 17.25784	20.75	20.95	20.53	20.14	19.82
341.69899, 6.94296	16.69	16.27	16.32	16.41	16.45	124.01025, 58.80669	21.7	21.44	21.32	21.19	20.99
266.94696, 55.48833	19.24	19.18	18.99	18.99	18.69	62.09121, 14.25436	22.33	22.25	21.51	21.33	20.62
20.50225, −8.56376	21.89	21.7	21.64	21.57	21.73	196.3116, 58.48208	19.09	19.28	19.27	19.12	19.04
356.00764, 0.3548	21.44	21.59	21.41	21.41	20.91	231.87791, 18.2909	19.69	19.96	19.68	19.53	19.47
321.60467, 20.33012	16.98	16.73	16.85	16.98	17.06	164.24258, 39.71087	20.09	19.59	20.92	20.71	19.38
324.25769, 7.24606	19	19.02	18.72	18.21	17.63	24.25438, −9.20979	19.28	18.98	18.58	18.18	17.88
310.89961, −5.88787	23.08	22.43	22.82	22.46	22.72	332.54138, 18.90505	19.66	19.81	19.45	19.11	18.77
335.43653, 18.66889	17.56	17.52	17.52	17.49	17.25	65.46418, 30.6942	19.55	18.92	18.48	18.3	18.04
323.97834, 23.61225	20.11	20.31	19.89	19.86	19.82	122.6726, −1.18979	19.95	20.11	19.98	19.94	19.6
327.2107, −2.1064	23.1	22.41	22.29	22.23	21.33	110.43529, 66.64391	16.66	16.44	16.56	16.69	16.81
239.23742, 35.39421	19.18	18.92	18.86	18.83	18.75	52.22918, 5.38163	19.06	18.96	18.7	18.58	18.48
335.43655, 18.66882	17.56	17.52	17.52	17.49	17.25	79.84544, 15.90972	18	18.12	17.62	17.38	17.15
320.16528, −16.79779	21.32	21.4	21.1	21.05	20.92	73.26087, 11.9668	19.07	18.25	18.04	18.01	17.91
155.11069, 53.07588	17.29	17.42	17.18	17.14	16.94	116.00201, 41.91769	20.74	20.51	20.69	20.78	20.48
254.51559, 14.60941	21.66	21.66	21.41	21.05	20.67	355.67641, 34.22522	23.27	23.7	22.05	23.54	22.94
230.96351, 8.60175	20.15	20.2	19.67	19.4	19.28	352.51261, 30.55014	19.3	19.48	18.9	18.46	17.93
341.90166, 25.07674	22.12	21.75	21.55	21.47	21.07	122.82138, 15.33414	22.18	22.19	22.45	22.38	22.7
321.72727, −1.34832	18.1	18.18	18.09	17.68	17.56	119.99694, 21.32674	23.46	22.67	23.05	22.96	23.71
208.57848, 27.60082	22.84	22.59	21.66	21.45	21.3	327.63934, 5.92634	18.75	19.33	19.22	18.96	18.83
260.26038, 27.55036	20.01	20.06	20.23	20.35	20.24	312.93942, 7.88469	25.1	22.57	23.47	24.27	23.38
251.20596, 19.99455	20.31	20.58	20.53	20.39	19.85	269.13878, 57.49082	20.52	21.05	20.8	20.56	20.43
323.60005, −7.98628	20.97	21.12	21.21	21.5	21.45	349.78824, 33.26105	17.45	17.79	17.68	17.36	17.02
234.63679, −15.28853	20.67	20.16	19.54	19.22	18.94	330.86617, 14.18294	21.64	21.77	21.8	21.6	21.54

Ra,Dec	u	g	r	i	z	Ra,Dec	u	g	r	i	z
71.42965, 11.14992	22.86	21.75	21.18	21.16	21.47	142.16386, 0.99579	21.7	21.8	21.69	21.18	21.05
245.54005, 36.07183	20.48	20.15	20.17	20.18	20.04	131.00039, 2.6552	18.21	18.33	17.94	17.57	17.3
27.71469, 33.43934	17.87	18.19	18.1	18.01	17.77	137.21738, 7.27777	20.55	20.13	20.28	20.26	20.2
330.0772, 25.76412	20.79	20.87	20.65	20.61	20.7	52.39128, 18.42499	20.43	20.5	20.4	20.14	19.83
326.91002, 24.76496	18.72	18.67	18.54	18.2	17.65	126.51549, 11.63922	20.49	20.63	20.54	20.44	19.99
86.49273, 2.35178	19.63	19.43	18.74	18.05	17.43	15.87079, 33.30612	18.48	17.98	18.12	18.27	18.34
85.39584, 1.61888	20.12	20.19	19.74	19.55	19.36	8.26665, 38.01821	20.85	20.73	20.73	20.58	19.84
311.34494, −1.16791	21.78	21.44	21.42	21.69	21.4	357.06133, 18.20544	18.27	17.99	18.1	18.19	18.25
26.40939, 28.36127	20.32	20.56	20.32	20.48	20.09	164.48463, 9.38752	16.54	15.88	15.21	14.91	14.76
54.29562, −6.84977	19.62	19.56	19.72	19.97	20.1	346.10793, 6.42945	21.34	21.09	20.99	21.36	21.11
331.67107, 30.24328	23.57	23.15	22.92	22.93	22.87	33.28321, 18.73771	21.18	20.8	20	19.53	19.16
1.83643, 20.12269	22.01	21.31	21.08	22.04	21.75	24.15423, 32.01113	14.47	14.3	14.38	14.44	14.51
242.10015, 16.87789	20.04	20.15	20.08	19.97	19.71	20.24844, 32.92911	20.36	20.09	20.24	20.52	21.22
232.59852, 22.11284	19.12	19.06	19.16	19.17	18.94	133.55818, 39.09367	19.65	19.15	19.22	19.23	19.13
310.74499, −0.56484	22.08	21.93	21.78	21.89	21.7	129.46223, 38.50361	19.11	19.18	19.2	18.63	17.96
338.3566, 4.65418	20.22	20.61	20.25	19.93	20.18	52.25848, 6.01296	22.9	22.04	21.58	21.11	20.53
313.21775, −6.24468	21.45	21.97	21.87	22	22.03	3.29428, 21.35224	18.61	18.58	18.71	18.89	19
332.23951, 20.0777	23.37	22.45	20.4	19.78	19.64	156.56682, 19.34577	20.11	20.13	20.08	19.85	19.51
216.45022, 15.25049	22.17	21.8	21.62	21.32	21.09	111.96763, 40.78124	21.55	21.45	21.58	21.32	21.05
307.2381, −6.30077	20.77	20.61	20.56	20.6	20.15	25.46001, 9.13933	19.92	20.06	19.98	19.97	19.93
224.84101, 35.80164	21.26	21.54	21.07	20.76	20.4	310.00584, −14.81902	20.4	20.56	20.49	20.44	20.3
326.66642, 9.35535	22.17	21.83	21.71	21.89	22.33	52.16604, −1.04452	20.96	21.13	20.93	21.06	20.68
225.6706, 33.57317	17.8	17.5	17.55	17.62	17.51	117.08311, 24.96631	22.61	22.51	22.9	22.36	22.26
247.0257, 6.88764	20.8	20.65	20.58	20.49	20.14	3.41491, 33.35653	23.1	22.02	21.83	21.92	20.8
205.77343, 52.1454	22.95	21.68	20.71	20.5	20.01	151.74333, 23.62341	18.45	18.31	17.93	17.52	17.14
146.65238, 44.7793	19.33	19.37	19.15	18.81	18.25	38.04864, 30.61	21.07	20.82	20.37	19.83	19.4
325.30462, −3.51307	17.83	17.7	18	18.19	18.38	337.57824, 29.48019	23.6	22.48	22.26	22.89	22.26
331.47492, 11.93162	20.12	20.03	20.06	20.19	20.22	14.60248, 28.55118	19.07	19.22	18.98	19.15	18.92
228.72342, 2.15946	15.57	15.45	15.75	15.98	16.18	315.14313, 5.91002	22.4	22.25	22.16	21.85	20.96
317.19351, −3.842	18.71	18.61	17.98	17.55	17.17	18.81888, 24.92506	21.45	21.24	21.24	21.15	20.64
135.06943, 34.65765	21.28	20.62	20.32	20.07	19.73	24.4051, 30.04685	17.77	17.49	16.77	16.45	16.27
248.16364, 35.18554	23.16	22.7	23.07	24.11	22.25	328.10701, −1.48061	24.88	21.38	19.82	18.42	17.71
139.29103, 31.71904	21.62	20.48	19.38	19.13	19.05	356.16903, −0.20135	21.23	21.09	21.06	20.74	20.02
236.43705, 44.47502	20.85	20.94	20.85	20.72	20.33	0.1028, 33.42861	20.7	20.76	20.53	20.4	20.04
204.92152, 48.79117	17.86	17.68	17.77	17.96	18.1	252.45992, 3.97634	18.86	18.55	18.59	18.53	18.34
255.46497, 13.35851	19.4	19.19	19.3	19.32	19.23	261.31463, 7.54693	20.48	20.66	20.61	20.73	22.38
118.56039, 31.53773	19.91	19.65	19.64	19.74	19.62	246.33463, 12.05252	18.12	18.53	18.41	18.21	17.72
230.49484, 26.20644	21.05	21.07	20.82	20.96	21.39	330.13013, 3.57514	18.55	18.66	18.4	18.13	17.94
120.76667, 25.27449	19.45	19.59	19.39	19.25	18.89	341.27236, 1.26317	21.44	21.55	21.54	21.66	21.22
116.66919, 17.57022	19.49	19.77	19.64	19.52	19.43	251.60326, 18.13568	21.66	21.09	20.86	21.17	20.7
120.7791, 28.81559	16.49	16.28	16.42	16.58	16.7	337.10045, 13.82892	22.7	22.34	22.44	22.6	22.43
137.94586, 31.85057	15.34	15.18	15.51	15.75	15.96	329.56373, 9.7859	17.59	17.48	17.61	17.55	17.15
186.92036, 51.65704	19.11	19.07	19.06	19.06	18.71	348.968, 27.17689	20.9	20.65	20.04	19.17	18.55
153.14108, 7.7807	15.64	15.41	15.78	15.95	16.13	246.82662, 12.07644	18.98	19.23	19.06	18.85	18.48
114.49393, 20.92909	17.2	17.4	17.22	17.28	17.27	170.7222, −11.17699	20.71	20.44	20.46	20.57	20.46
230.15777, 4.16326	16.18	16	16.31	16.51	16.67	1.7483, 19.4716	21.18	21.36	21.01	21.02	20.63
171.29032, 23.17672	20.57	20.99	21.06	21.3	20.46	248.29727, −1.19212	21.17	21.36	21.09	21.15	20.76
171.95302, −5.70941	20	20.12	20.09	20.28	20.15	239.18439, −0.16401	18.18	18.25	18	17.9	17.51

Ra,Dec	u	g	r	i	z	Ra,Dec	u	g	r	i	z
205.21693, 15.22806	20.26	18.73	17.99	17.72	17.57	26.79053, 17.25556	15.04	14.88	15.13	15.28	15.43
235.97547, −14.6291	21.22	21.4	21.09	21	20.53	68.94525, 9.14356	21.94	21.83	21.42	21.21	20.73
258.0122, 27.90305	17.51	17.3	17.53	17.67	17.85	28.93092, 0.46871	19.52	19.31	19.02	18.79	18.67
135.96135, 33.01002	18.85	18.83	18.79	18.88	18.62	324.90657, −2.65352	20.2	20.01	19.87	19.64	19.21
130.28376, 10.42683	19.82	20.25	20.13	20.02	20.05	121.11848, 36.51784	22.23	22.11	21.88	21.45	21.24
341.97463, 23.92265	21.66	21.5	21.28	21.4	21.1	351.4644, −1.67327	18.48	18.85	18.21	17.94	17.72
339.79081, 25.05861	19.16	19.16	19.05	18.89	18.8	117.74988, 14.19728	19.2	19.09	18.98	18.79	18.59
326.11012, 22.3401	18.91	17.64	17.13	16.98	16.91	113.41366, 21.36699	20.83	20.45	19.62	19.11	18.78
338.14024, 18.84335	20.07	20.6	20.37	20.48	20.4	319.69162, 12.09676	18.77	18.24	18.38	18.49	18.58
332.86967, −3.08772	19.65	19.55	19.46	19.46	19.13	342.06031, 33.20674	21.05	20.94	20.87	20.79	20.58
251.9499, 43.64583	21.4	21.54	21.82	22.27	21.77	337.22383, 29.85402	23.31	23.49	23.61	22.67	22.31
247.12867, 24.0498	20.14	20	19.83	19.66	19.46	78.5828, 1.18913	20.25	20.51	20.26	20.13	19.85
174.28592, 51.58081	21.1	20.67	20.08	19.95	19.74	347.92822, 20.67667	20.63	20.54	20.25	20.03	19.7
321.6389, 8.91643	20.49	20.76	20.74	20.55	20.25	9.69252, 19.11324	26.46	22.67	21.25	20.03	19.2
134.01571, 32.35255	19.5	19.64	19.74	19.77	19.62	116.082, 32.91337	20.73	20.76	20.7	20.83	21.02
239.45012, 7.09529	22.62	22.81	22.94	23.48	21.86	336.45026, 25.4198	20.14	20.2	19.96	19.25	18.75
232.56262, 9.82956	18.39	18.87	18.47	18.47	18.52	53.70755, −7.1799	14.9	14.59	14.83	15.02	15.19
231.25732, −1.50586	23.1	22.68	22.61	23.82	22.41	12.97035, 20.67151	18.96	19.06	18.37	17.94	17.55
224.43649, 40.72794	19.34	19.32	19.31	19.15	18.77	65.62201, 16.24169	22.85	21.96	21.44	20.92	20.35
172.84335, 43.37722	15.81	16.14	15.93	15.89	15.96	119.30758, 22.38142	21.01	21.3	21.2	21.1	21.42
124.65348, 1.36865	24.21	24.63	23.18	22.64	22.76	136.31687, 12.08089	19.5	19.75	19.72	19.59	19.68
238.91769, 36.77878	20.47	20.81	20.96	20.77	20.49	331.20731, 5.81453	21.2	20.94	20.72	20.14	19.65
118.38325, 37.96682	21.27	21.33	21.3	21.2	20.59	315.52371, 2.97622	21.74	21.48	21.4	20.86	20.39
223.75931, 14.63762	20.24	20.49	19.94	19.48	19.12	339.99297, 34.38475	25.45	22.4	22.51	22.79	22.28
317.47553, 16.51445	19.13	19.52	19.32	19.19	19.09	16.45873, 19.05477	19.42	19.64	19.82	19.96	19.98
239.23735, 35.39392	19.18	18.92	18.86	18.83	18.75	340.95194, 8.15752	19.3	19.55	19.33	19.25	18.7
156.65432, 47.9073	20.24	20.13	20.18	20.32	20.03	16.04836, −3.22818	19.02	19.52	19.14	18.83	18.9
64.15361, 29.46837	22.28	22.25	21.36	20.79	20.32	252.51159, 43.9377	22.33	22.76	22.34	21.87	21.3
66.12747, 29.44519	24.22	23.1	22.87	24.05	22.3	123.03182, 13.30685	19.22	19.27	19.16	19.03	18.67
139.14434, 13.06606	21.38	21.89	21.55	21.92	21.63	344.68116, 11.15324	14.07	13.86	15.08	14.15	14.18
134.02847, 12.6435	22.39	22.42	22.16	22.28	22.2	333.8324, −0.54908	17.54	17.38	17.49	17.59	17.67
138.96532, 9.01377	15.42	14.74	15.54	14.86	14.69	346.79727, 29.66957	22.2	21.5	20.68	19.93	19.41
61.74923, 0.87886	18.08	18.39	17.75	17.52	17.3	12.03004, 26.77259	21.33	21.57	21.31	21.45	22.29
51.7154, 1.25368	24.39	22.67	21.26	20.58	20.08	316.71066, 11.04723	19.78	20.24	20.16	20.14	19.8
69.62126, 0.67108	19.43	19.49	19.4	19.28	19.04	241.07934, 16.26361	18.68	19.08	18.82	18.75	18.73
161.04761, 21.21863	19.2	19.35	19.26	19.48	19.27	139.21135, 28.8287	18.94	19.16	18.52	18.19	17.89
55.04233, 39.21259	25.65	23.44	25.15	24.17	21.88	36.6347, 21.11495	21.4	21.97	20.68	20.25	20.86
124.90027, 19.26115	20.88	20.36	19.94	19.75	19.91	333.43348, 17.54776	19.1	19.26	19.21	19.16	18.87
163.77913, 36.99602	20.38	20.27	20.34	20.62	20.64	355.85354, 42.14485	20.25	20.18	19.89	19.6	19.19
220.81889, −1.03946	21.71	22.18	21.93	21.91	21.82	112.73136, 42.9432	22.39	22.76	23.02	23.3	21.78
22.15971, 18.75991	22.91	21.68	21.55	22.02	21.96	337.89994, 18.12964	21.23	21.66	21.41	21.5	21.77
89.67826, 0.10721	20.62	20.33	18.98	18.43	17.93	333.13329, 16.02786	19.05	19.11	18.86	18.59	18.29
57.51434, 37.01441	19.39	18.94	18.82	18.87	18.84	338.57698, −3.92503	20.42	20.5	20.19	19.91	19.59
122.62756, 0.40795	19.28	18.91	18.7	18.84	18.77	27.96621, 14.01333	19.98	20.28	19.98	19.57	19.13
80.96569, 1.0085	16.61	16.69	16.54	16.3	16.08	318.96194, −0.12105	24.02	23.31	23.2	22.76	21.53
11.6072, 38.34009	25.58	22.53	22.19	21.49	21.23	339.99268, 23.31037	22.73	22.14	21.92	21.86	22.94
124.30103, 5.86888	21.84	21.39	20.86	20.61	20.2	263.28287, 30.10959	22.71	22.53	22.35	21.94	21.01
125.08071, 47.7921	21.27	21.36	21.31	21.3	20.89	265.53823, 23.8082	19.75	19.7	19.47	19.26	18.86

Ra,Dec	u	g	r	i	z	Ra,Dec	u	g	r	i	z
256.76024, 16.89408	21.2	21.59	21.23	21.03	20.52	44.06248, 19.26978	25.41	23.9	22.85	22.74	23.37
320.10466, 19.69909	21.82	21.82	21.81	21.64	22.73	132.78084, 3.14291	18.7	18.77	18.85	18.83	18.6
244.82378, −2.4915	17.39	17.3	16.82	16.6	16.52	30.23343, 19.95745	20.01	19.28	19.37	19.45	19.77
329.1269, −3.33236	21.71	22.14	21.8	22.11	22.02	201.40007, 21.01027	22.13	23.07	20.38	20.64	20.57
242.61513, 9.12737	20.17	20.1	20.05	20.25	20	345.92405, 17.29861	19.79	19.84	19.62	19.42	19.25
327.49974, 12.75792	22.24	21.93	22.04	21.89	22.14	231.90315, 16.73499	24.29	23.38	24.4	24.79	22.64
264.7126, 29.38722	20.62	21	20.46	20.32	20.15	335.00946, 11.64038	21.12	21.37	20.64	20.31	20.09
208.07909, 28.15477	20.7	20.67	19.93	19.58	19.22	19.05736, 9.37115	19.04	19.13	19.03	18.82	18.62
354.70279, 28.33195	18.34	18.54	18.05	17.9	17.85	18.93017, 33.62338	20.39	20.56	20.29	20.11	19.54
340.72257, 17.42727	17.6	17.54	17.56	17.68	17.83	69.42534, 0.51329	20.69	20.35	21.52	20.76	20.01
329.15135, 19.54498	18.92	18.78	18.49	18.35	18.07	64.39407, −6.23257	22.26	22.73	22.99	21.61	24.65
189.6402, 3.31512	22.26	21.56	21.33	21.14	21.36	324.94631, 17.11613	18.12	17.71	17.81	17.91	18
315.1831, −0.86992	21.26	21.61	21.51	21.06	21.01	6.25075, 7.5638	19.25	19.68	19.21	18.93	18.73
253.49575, 20.16956	18.46	18.66	18.42	18.26	18.17	323.6346, −1.34447	23.61	23.25	23.31	23.51	23.25
255.31589, −2.69957	24.05	22.98	22.25	22.29	22.84	174.9608, 45.97172	19.57	19.62	19.49	19.35	18.85
170.88349, 43.28819	19.43	19.91	19.75	19.64	19.47	338.14767, 30.68472	22.43	22.47	22.41	22.05	21.75
231.55824, 8.30052	17.8	17.8	17.82	17.72	17.41	52.76843, 17.4278	19.98	19.86	19.32	18.88	18.47
245.64892, 3.87959	22.36	22.24	21.73	21	20.29	138.72327, 11.56717	21.23	20.97	21.05	21.19	21.31
336.85203, 28.73439	18.23	18.56	17.99	18	17.79	11.25127, 22.45222	20.2	20.45	20.21	20.13	19.66
220.04601, 49.79271	21.25	21.16	21.01	21.5	22.61	342.0986, −9.34962	21.14	21.13	21.17	21.08	20.82
130.36405, 21.01488	20.59	20.61	20.4	20.08	19.64	322.60263, −2.98824	17.43	17.61	16.99	16.49	16.12
258.09622, 36.42107	20.78	20.88	19.9	19.44	19.26	164.64614, 5.7851	20.14	20.4	20.24	20.15	19.94
159.41103, 12.71394	22.11	21.9	21.77	21.63	20.93	17.89353, 27.98938	21.62	19.97	19.83	20.03	20.58
192.08069, 7.34719	21.66	21.33	21.4	21.39	21.28	11.32644, 18.89707	21.77	21.05	20.6	20.46	20.26
157.94998, 8.87347	18.8	18.8	18.76	18.56	18.29	238.62739, 36.84519	21.78	21.7	21.52	21.56	22.09
153.94117, 3.55329	19.81	20.17	20.14	20.13	19.86	351.58093, 28.4472	20.88	20.89	20.54	20.58	20.19
316.76889, 1.73774	23.38	23.89	23.09	23.67	23.54	67.58311, 9.88828	20.75	20.38	19.64	19.09	18.65
232.24115, 3.81994	19.08	19.51	19.35	19.17	19.09	17.99, 35.29008	18.72	18.72	18.47	18.14	17.66
246.58264, −12.93237	21.83	21.6	21.13	20.9	20.56	345.31418, 22.68647	23.71	22.11	22.04	21.74	22.1
165.06137, 13.26448	18.32	18.65	18.78	18.55	18.37	18.27812, 21.88067	20.5	20.41	20.19	19.9	19.51
244.78793, 13.86267	18.9	18.49	17.8	17.43	17.17	16.34257, 11.04802	20.64	20.71	20.56	20.28	20.08
251.05522, 5.69954	16.98	16.81	16.98	17.14	17.28	310.29216, −4.63406	25.03	22.79	22.71	22.08	21.86
65.42558, 34.05791	22.55	22.43	21.9	21.44	20.84	195.12633, 11.85039	19.89	19.78	19.8	19.84	19.42
151.31405, 19.18552	18.09	18.17	18.25	18.12	17.82	164.23779, 49.68854	17.48	17.77	17.52	17.34	17.18
154.94695, 33.96506	17.85	18.39	18.2	18.07	17.9	211.22493, −10.45056	20.02	19.73	19.86	19.87	19.58
117.36669, 19.08112	20.55	21.12	20.89	20.83	20.32	339.02617, 5.08794	22.41	22.3	22.38	22.57	22.29
130.17273, 0.08894	20.54	20.79	20.8	21.01	20.64	345.96517, 1.11426	17.83	18.27	18.01	17.75	17.56
131.05687, −1.46866	20.31	20.11	20.13	20.17	20.18	250.44488, 12.17383	21.22	21.36	21.13	20.59	20.72
231.08042, 22.15563	19.03	19.05	18.9	18.81	18.5	245.84263, 12.22613	17.09	16.98	17.12	17.22	17.32
236.11716, 33.95692	22.36	22.11	21.85	22.28	21.61	246.52379, 22.84566	22.29	22.68	22.25	22.09	21.54
121.87372, 15.57832	22.19	22.48	22.06	22.05	22.2	227.58642, 18.38403	21.46	21.42	20.69	20.49	20.24
160.21344, 15.19271	18.23	17.97	17.53	17.19	17	321.47946, −3.40165	22.4	22	22.13	23.48	21.14
129.6883, 49.18208	19.2	19.58	19.37	19.35	19.08	133.53919, 20.22756	20.31	20.91	20.48	20.32	20.11
125.34891, 45.69314	19.23	19.47	19	18.82	18.65	247.83706, 10.52608	18.17	19.03	18.56	18.43	18.46
155.83452, 44.0861	18.53	18.85	18.7	18.59	18.51	327.01833, 8.16404	20.54	20.96	20.88	20.69	20.43
68.82405, 0.49468	21.89	21.96	22.14	22.71	22.09	212.50921, −12.80243	17.85	17.65	17.85	18.02	18.11
256.54032, 14.58111	17.73	18.23	17.9	17.71	17.71	337.74302, 21.02971	20.69	20.79	20.68	20.79	20.25
12.25832, 7.79058	21.74	21.52	21.49	21.79	22.14	246.25717, 39.1573	17.08	17.19	17.09	16.99	16.83

Ra,Dec	u	g	r	i	z
249.52245, 8.63291	20.41	19.74	19.04	18.6	18.42
241.35058, 6.13773	22.54	22.82	22.56	22.07	22.58
234.14338, 33.48113	18.98	19.21	18.94	18.76	18.59
191.07451, 30.06699	18.56	18.6	18.51	18.39	18.11
246.73667, −0.43016	22.22	22.61	22.35	21.78	21.69
214.29992, −18.0577	20.44	20.62	20.27	20.06	19.52
240.63397, 16.29236	22.54	21.91	21.78	21.84	21.33
238.35696, 11.74355	23.17	23.24	23.89	22.93	23.02
122.22386, 35.84814	19.55	19.66	19.61	19.52	19.3
245.05002, 11.88252	19.71	19.36	19.64	19.73	19.97
266.80973, 15.01325	17.52	17.31	17.44	17.52	17.59
123.57877, −0.83948	18.93	19.12	18.97	18.79	18.51
119.20008, 30.96818	21	20.86	20.93	20.87	20.88
323.2893, 15.83453	22.38	22.07	21.93	21.41	21.2
240.01546, 33.18719	19.88	19.88	19.86	19.66	19.23
132.80597, 34.74687	20.55	20.45	20.5	20.03	19.34
232.96166, 15.41301	20.34	20.13	20.19	20.3	20.5
240.52, 3.27549	23.41	23.22	22.84	22.49	22.19
218.75094, −0.76842	18.43	18.56	18.42	18.4	18.35
130.99192, 42.84368	19.6	19.91	19.88	19.69	19.3
89.37526, 0.25384	25.01	22.92	22.07	21.87	22.03
126.72785, −0.12581	19.85	19.52	19.5	19.64	19.61
157.40711, 41.67956	22.21	22.27	22.32	23.09	22.01
122.19245, 31.51837	19.12	19.43	18.75	18.17	17.74
135.66542, 5.41683	23.77	23.16	23.06	23	22.13
114.83817, 22.415	22.78	22.7	22.38	22.13	22.53
242.18662, 22.10279	21.17	21.64	20.97	21	20.9
123.04267, 4.0644	22.43	22.61	22.43	21.78	20.99
200.26325, 1.89144	19.47	19.18	19.21	19.34	19.37
171.64158, −10.03616	18.81	18.81	18.62	18.37	18.13
136.61769, 5.44915	18.82	18.76	18.45	18.1	17.83
131.47937, 3.65813	20.57	20.59	20.6	20.86	21.03
158.32188, 7.3552	19.94	19.89	19.81	19.75	19.48
80.14105, −0.09169	20.76	20.52	19.74	19.27	18.87
123.56217, 8.08062	21.97	22.23	22.05	21.59	21.09
178.37594, 31.97667	20.69	20.11	19.94	19.9	19.97
249.92791, 12.404	19.37	19.48	19.21	19.07	18.96
137.46048, 18.82975	15.91	16.03	15.7	15.33	15
32.79259, 17.27342	19.44	19.4	19.18	19.02	18.71
163.95866, 9.93904	19.03	19.15	18.51	17.88	17.4
351.32998, −8.30523	19.04	19.1	18.93	18.66	18.14
127.09064, 10.89569	22.11	22.29	22.08	22.22	22.13
190.11424, −15.09947	21.33	21.02	20.77	20.6	20.33
137.26825, 9.28709	22.32	22.47	22.1	21.57	21.22
327.17719, −0.12319	23.41	22.68	22.97	23.32	22.39
70.56681, −0.39275	22.23	21.93	21.73	21.85	21.99
134.59523, −0.62471	22.53	22.34	22.04	21.98	21.6

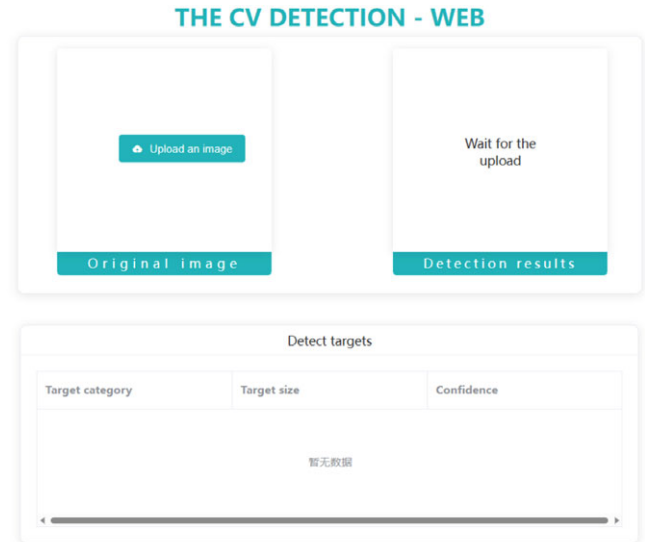## Appendix B. The CV detection toolkit

Figure B1. The user interface of CV detection toolkit.
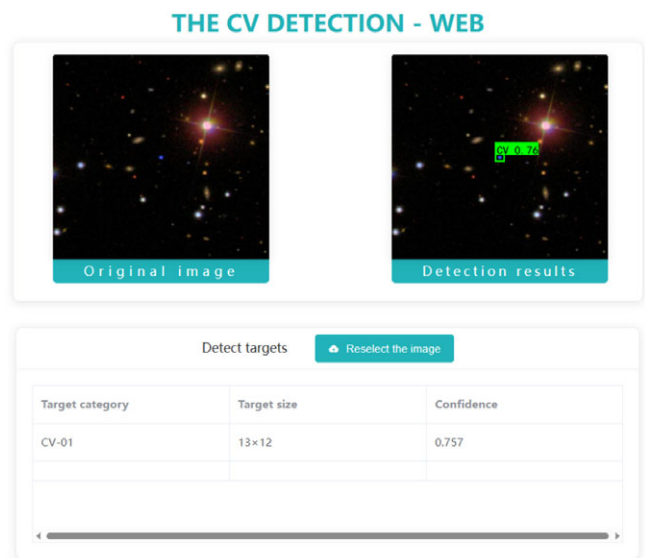

Figure B2. The detected result display of an upload image by the trained improved YOLOX model.